



Cite this: DOI: 10.1039/d5ta03380b

Nanostructure-dependent lattice oxygen reactivity and degradation of CoNi oxyhydroxide OER electrocatalysts: a mechanistic study†

Liyuan Ran,^{‡a} Kai Zhao,^{‡a} Xiaoyi Jiang^{‡a} and Ning Yan^{ID*ab}

The development of efficient catalysts is crucial for generating green hydrogen *via* water electrolysis. Nanostructured electrodes are promising candidates which enjoy a high surface area and abundant active area, affording high current density with low polarization loss. Yet, they are often less stable than the bulk counterpart, which suffers from structural disintegration and performance degradation during the longevity test. Herein, to understand the mechanism of such instability, we prepared a series of CoNi oxyhydroxide nanostructures as model catalysts for the oxygen evolution reaction (OER) and examined their structural degradation mechanism under *operando* conditions. The nanorod with a lower height showed faster performance degradation rate and severe structure disintegration, whereas the nanosheet is rather stable during the OER. Interestingly, in the examination of lattice oxygen reactivity using differential electrochemical mass spectrometry coupled with ¹⁸O isotopic labeling, the tetramethylammonium cation (TMA⁺) probe molecule and proton reaction order plot, we found that the OER pathway differed among these nanostructures, showing a prominent structure-dependent lattice oxygen reactivity which is strongly correlated with the structural stability of model catalysts. Our finite element analysis also indicated that the high local reaction rates at the tip of the nanorod with a large curvature exacerbated the electrode corrosion. This work reveals the structure-dependent lattice oxygen reactivity in oxyhydroxide OER catalysts, offering guidelines for developing robust electrocatalysts for real-life applications.

Received 29th April 2025

Accepted 10th July 2025

DOI: 10.1039/d5ta03380b

rsc.li/materials-a

1. Introduction

The global overconsumption of fossil fuels has led to energy shortages and severe environmental damage, necessitating the urgent development of alternative energy technologies and a reduction in fossil fuel dependence.^{1–4} In this context, green hydrogen, which is produced *via* water electrolysis using renewable energy, becomes an ideal energy carrier. Due to the sluggish kinetics of the oxygen evolution half-reaction (OER) at the anode, it remains critical to employ high-performance electrocatalysts such as precious metals in order to achieve high efficiency. Recently, cobalt-, nickel-, and iron-based electrocatalysts have garnered significant attention due to their high activity, low cost, and earth abundance.^{5,6} Defect-rich nanostructured designs in these materials can provide abundant active sites, enhance the catalytic surface area, and improve the overall electrochemical performance.^{7–9} However,

a critical challenge persists: nanostructures often collapse easily under *operando* conditions through various ways, including elemental leaching, phase transition and corrosion.^{10,11} This inevitably causes rapid catalyst deactivation, precluding their large-scale application in practice.

Investigating the causes of electrocatalyst deactivation is a critical focus in current research, as understanding these mechanisms is essential for designing catalysts that balance activity and stability.^{12,13} Electrocatalyst deactivation occurs in both acidic and alkaline environments, although studies under acidic conditions are more extensive.^{14,15} In acidic media, deactivation mechanisms are well-documented and primarily attributed to the H⁺-induced corrosion where proton attack leads to severe metal dissolution and structural disintegration.¹⁴ Besides, the reconstruction can cause phase and/or morphological changes, leading to the decrease of a number of active sites.^{16,17} In some cases, the acidic media can also passivate the catalyst surface, generating an inert surface with impaired catalytic activity.¹⁸ Under alkaline conditions, catalyst deactivation predominantly stems from the progressive leaching of metallic species at elevated potentials, ultimately compromising catalytic stability.¹³ This phenomenon is particularly pronounced in electrocatalysts with reactive lattice oxygens during the catalysis. The irreversible structural

^aSchool of Physics and Technology, Wuhan University, Wuhan, China. E-mail: ning.yan@whu.edu.cn

^bShenzhen Research Institute of Wuhan University, Shenzhen, 518057, China

† Electronic supplementary information (ESI) available. See DOI: <https://doi.org/10.1039/d5ta03380b>

‡ These authors contributed equally to this work.

reconstruction—triggered by lattice oxygen exchange—induces sustained metal depletion, thereby accelerating durability degradation.^{19,20} For instance, Schmidt *et al.* elucidated the inherent instability of metal oxides during the OER in alkaline media, attributing this behavior to the synergistic effects of high anodic potentials and corrosive electrolyte interactions. Under such conditions, oxidative dissolution is markedly intensified, driving dynamic yet irreversible catalyst reconstruction through concurrent oxidation, dissolution, and redeposition processes.²¹ Crucially, the evolution of lattice oxygen generates abundant oxygen vacancies, which precipitate structural collapse and perpetuate metal leaching, culminating in progressive catalyst deactivation.^{22,23} These mechanistic insights are pivotal for guiding the rational design of stable and active electrocatalysts.

In this work, we prepared a series of CoNi oxyhydroxide nanorod OER catalysts with different aspect ratios as the model systems and examined their structural degradation mechanism under *operando* conditions. The catalyst with a higher aspect ratio showed faster performance degradation rate and severe structure disintegration during the OER at a constant current density, whereas the nanosheet control with an aspect ratio of ~ 1 shows essentially no performance/structural change. Interestingly, in the examination of lattice oxygen reactivity using differential electrochemical mass spectrometry (DEMS) coupled with ¹⁸O isotopic labeling, the tetramethylammonium cation (TMA⁺) probe molecule and proton reaction order plot, we found that the OER pathway differed among the nanostructures, showing a prominent structure-dependent lattice oxygen reactivity which is strongly correlated with the structural stability of model catalysts. Our finite element analysis (FEA) also indicated that the high local reaction rates at the tip of the nanorod exacerbated the electrode corrosion.

2. Experimental

2.1. Sample preparation

All model catalysts were deposited onto the nickel foam *via* a hydrothermal synthesis method. The nickel foam was first cut into $2 \times 2 \text{ cm}^2$ pieces and placed into a beaker. An appropriate amount of deionized water (DIW) was added, followed by a few drops of concentrated hydrochloric acid. The beaker was then sealed and subjected to ultrasonic treatment for 30 minutes. Afterward, the solution was discarded, and the obtained nickel was rinsed with DIW. Then, anhydrous ethanol was added into the beaker for another 15 minutes of ultrasonic cleaning. The cleaned nickel foam was finally rinsed with deionized water under ultrasonic treatment for 15 minutes and then dried in an oven.

The CoNi model catalysts (the molar ratio of Co : Ni was 2 : 1) were synthesized by a one-step hydrothermal synthesis method. All chemicals were analytically pure and used without further purification. First, 0.522 g of $\text{Co}(\text{NO}_3)_2 \cdot 6\text{H}_2\text{O}$, 0.261 g of $\text{Ni}(\text{NO}_3)_2 \cdot 6\text{H}_2\text{O}$ and 0.504 g of urea were added into the beaker and dissolved in 30 ml DIW. The solution was thoroughly stirred for 30 min with a magnetic stirrer until a clear light-pink solution was formed. The solution was then transferred into

a 50 ml Teflon lined stainless steel autoclave where a piece of pretreated nickel foam was added. To obtain different nanostructures, the hydrothermal reaction was carried out at different temperatures for varied durations of time following an established procedure which was reported previously.²⁴ After the hydrothermal reaction, the nickel foam, which was covered by nanostructured CoNi carbonate hydroxides, was retrieved and then rinsed with DIW several times. The conversion of hydroxide to oxyhydroxide was performed under *operando* conditions during the electrochemical test.

2.2. Materials characterization

The morphology of CoNi catalysts was characterized using a Carl Zeiss GeminiSEM 500 scanning electron microscope with a resolution of 0.5 nm@15 kV. The transmission electron microscopy (TEM) study was carried out using a JEM-F200 microscope. X-ray diffraction (XRD) was performed *via* a Rigaku SmartLab X diffractometer. The radiation source was a copper target and the X-ray wavelength was $\lambda = 0.154 \text{ nm}$. The X-ray photoelectron spectroscopy (XPS) analysis was carried out using a K-Alpha spectrometer from the Thermo Fisher Scientific, where the Al $K\alpha$ ($h\nu = 1486.6 \text{ eV}$) X-rays were used to excite the photoelectrons. The ¹⁸O isotopic labeling coupled with DEMS was performed with a DEMS instrument which consists of a PrismaPlus quadrupole mass spectrometer from Pfeiffer Vacuum and a custom-built Swagelok cell. The system is equipped with a turbo vacuum pump (HiPace® 80, Pfeiffer) and a condenser to remove water vapor. In the customized DEMS cell, the model catalyst coated Ni foams were used as the working electrode directly.²⁵ The assembled WE was placed on a piece of PTFE which separates the electrolyte from the vacuum environment. A Hg/HgO electrode was used as the reference electrode (RE). Both the counter electrode (CE) and the RE were positioned above the WE within the same compartment.

2.3. Electrochemical tests

All electrochemical tests in this work were carried out using a CHI 760E electrochemical workstation (Shanghai Chenhua Instrumentation Co., Ltd). Linear scanning voltammetry (LSV), cyclic voltammetry (CV), and electrochemical impedance spectroscopy (EIS) were performed on the model electrocatalysts. The scan rate in the voltametric test was set at 1 mV s^{-1} . In the 3-electrode setup, a Hg/HgO electrode and a platinum sheet were used as the working electrode and counter electrode, respectively. Other than specified, the electrolyte was 1 M KOH aqueous solution maintained at 25 °C. All reported potentials were *versus* the reversible hydrogen electrode (RHE) which was converted using the equation below:

$$E_{\text{RHE}} = E_{(\text{Hg}/\text{HgO})} + 0.0591 \times \text{pH} \quad (1)$$

For all reported potentials in this work, post-*iR* compensation was applied at 95% value of the solution resistance, which was obtained from the EIS:

$$E_{\text{compensated}} = E_{\text{measured}} - iR \quad (2)$$

3. Results and discussion

3.1. Distinct behaviors of nanostructured OER catalysts

The schematic illustration in Fig. 1a shows nanostructured CoNi based model catalysts with different aspect ratios. They are denoted as CoNi-500-50, CoNi-650-50, CoNi-750-50, and CoNi-900-800, respectively. The first digit shows the height in nanometer, whereas the last digit shows the width at the bottom of the nanostructure in nanometer. The aspect ratios are 0.10, 0.07, 0.06 and 0.9, respectively. These model catalysts are subjected to the OER test, where the catalytic activity and stability together with the post-test structural integrity are examined. To probe the degradation mechanism, we also used various approaches to investigate the reactivity of lattice oxygen among the catalysts.

Fig. 1b–e show the SEM images of model catalysts with various aspect ratios. The Ni foam is fully covered by CoNi carbonate hydroxide nanorods after the hydrothermal synthesis. With the gradual increase of the reaction time under controlled temperature conditions, both the length and the width of the nanorods grow, yet the growth rate of crystals along the length direction is much faster where preferred crystal orientation presents.^{26,27} When the reaction time reaches 12 h, the crystal growth along the length direction is suppressed, and a nanosheet structure (CoNi-900-800) is formed. In the TEM micrographs shown in Fig. S1,† the nanorod structure is also clearly visible. The diameter of the rod is approximately 50 nm. The measured *d*-spacing is 0.264 nm, corresponding to the (221) plane of Co(OH)(CO₃)_{0.5}, the readily formed pre-catalyst during the hydrothermal synthesis. Besides, the energy dispersive X-ray spectroscopy analysis in Fig. S2† confirms the uniform distribution of Co and Ni species.

We then evaluated the OER performance of these model catalysts using the standard 3-electrode system in 1 M KOH. The anodic oxidation bumps starting at approximately 1.3 V (*vs.*

RHE and hereafter) in the linear sweep voltammograms (LSVs) in Fig. 2a correspond to the oxidation of Co²⁺ species. Among them, CoNi-750-50 shows the optimal OER performance with the lowest overpotential of 228 mV at the benchmark 10 mA cm⁻² (η). In comparison, CoNi-900-800 shows the highest η of 251 mV. The activity trend aligns with the electrochemical impedance spectroscopy (EIS) measurement recorded at 1.5 V. In the Nyquist plots shown in Fig. 2b, CoNi-750-50 also demonstrates the lowest charge-transfer resistance, thanks to the fast reaction at the electrode–electrolyte interface.

To understand the origin of activity among the model catalysts, we measured the electrochemical active surface area (ECSA) based on determining the double layer capacitance in the potential range where no faradaic processes occur (see Fig. 2c). This method is frequently applied to nanostructured materials in the literature using cyclic voltammetry (CV, see all plots in Fig. S3†). Not surprisingly, CoNi-750-50 shows the largest ECSA due to its large aspect ratio. CoNi-650-50 and CoNi-900-800 have a similar ECSA despite their rather distinctive nanostructures. The important electrochemical performance indicators are summarized in Fig. 2d.

We then performed the longevity test in a two-electrode system under a constant current. Indeed, all model catalysts show performance degradation during the OER (see Fig. 3a). CoNi-500-50 was completely deactivated after 200 h. The sudden voltage rise is attributable to the loss of electrode materials due to dissolution and delamination. This speculation is supported by the SEM image in the inset, showing that the spent catalyst suffers from severe dissolution and structural collapse, and no nanorods can be identified. The overpotential at 10 mA cm⁻² increases dramatically to >350 mV (see Fig. 3b). Similar performance and structural deterioration, although slightly gentle, are also notable in CoNi-650-50. CoNi-750-50 is more robust, which shows relatively stable voltage during the first 300 h of operation. The tip of the nanorod dissolves, yet the bottom structure remains, intact as shown in the SEM image. The OER overpotential at 10 mA cm⁻² increases to 289 mV after the longevity test. Conversely, both the activity and structure of CoNi-900-800 are stable during the 500 h test. The nanosheet structure is completely preserved despite the minor dissolution at the edge. The overpotential at 10 mA cm⁻² becomes 277 mV, which is the lowest among all spent catalysts. A detailed comparison of the overpotential change is shown in Fig. 3b.

We then characterized the spent catalysts in detail. Fig. 3c shows the XRD patterns of all model catalysts, retrieved from the electrode, after the stability test. Cobalt carbonate hydroxide is identified in all samples, which pertains to the presence of a pre-catalyst that has not been reconstructed under *operando* conditions to form the (CoNi)OOH active phase (see the Experimental for details). They are encapsulated by the oxyhydroxide film on the surface and are inaccessible by the electrolyte. We cannot find the presence of oxyhydroxide from the patterns, possibly due to its thin-film nature on the surface of the nanostructure. This inference is further supported by the XPS investigation in which the Co 2p core-level spectra of all spent catalysts show the presence of plenty of oxyhydroxide moieties.

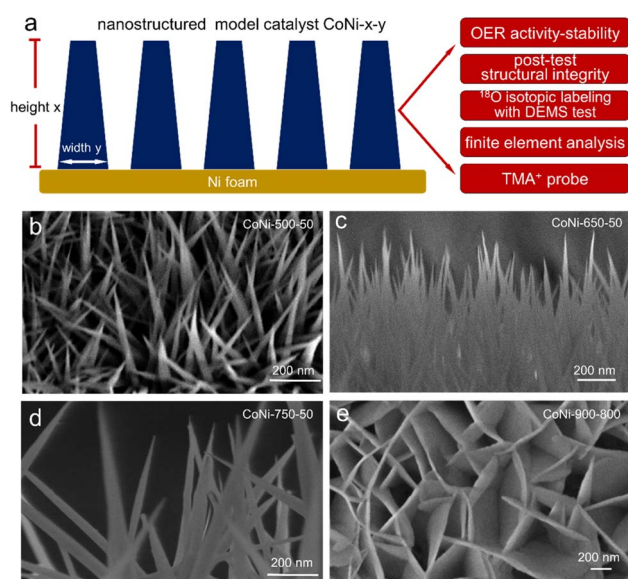


Fig. 1 (a) The schematic illustration of model catalysts with different nanostructures; (b–e) the SEM images of all model catalysts.

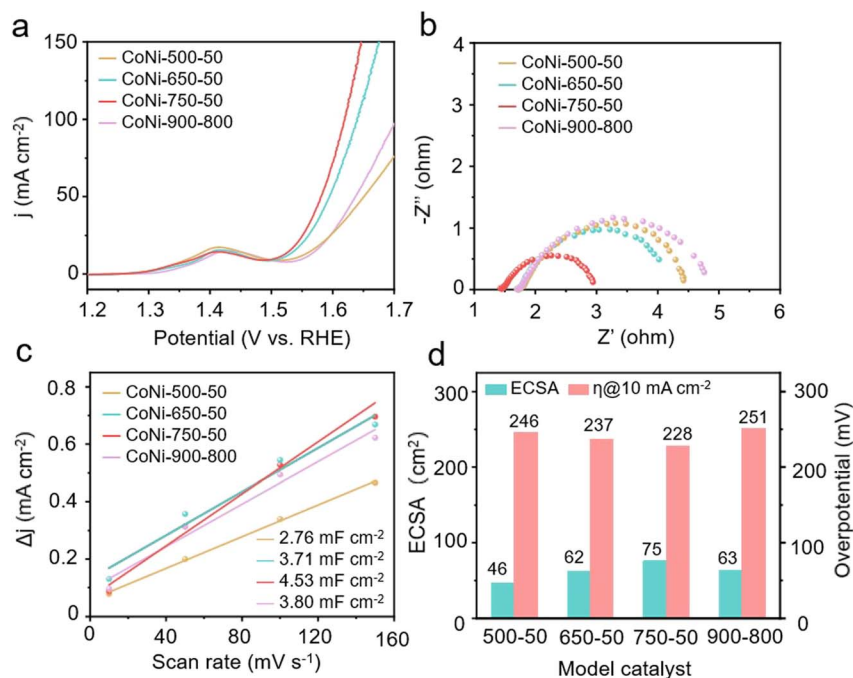


Fig. 2 (a) Linear sweep voltammograms, (b) Nyquist plots at 1.5 V vs. RHE, (c) double layer capacitance plots and (d) comparison of key electrochemical performance indicators of all model catalysts.

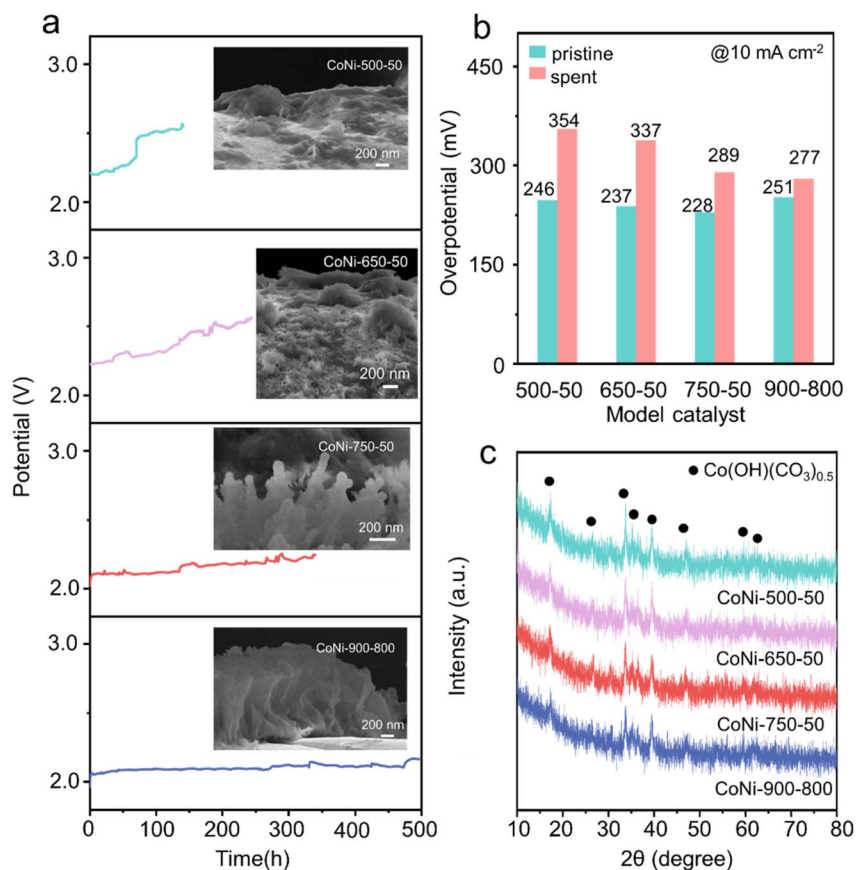


Fig. 3 (a) The longevity test at 200 mA cm⁻² of different model catalysts and the SEM image of the spent catalysts; (b) comparison of the OER overpotential at 10 mA cm⁻² for pristine and spent catalysts; (c) XRD patterns of the spent catalysts.

3.2. Understanding the nanostructure-dependent degradation

On the basis of the above results, we found that the nanostructures with identical chemical composition exhibit rather distinct degradation behaviors during the OER. To fundamentally understand the difference, we first performed finite element analysis (FEA) of different nanostructures during the OER. It simulates the Helmholtz layer based on the Nernst–Planck equation, Butler–Volmer equation and Gouy–Chapman–Stern model. The current density distribution in the nanostructure is illustrated in Fig. 4a–d. At the tip of the nanorod, the current density is nearly two orders of magnitude higher than that at the bottom region. Similar effect is also obvious at the top of the nanosheet structure and in the literature.^{28,29} This inhomogeneity reflects the fact that the top region of the nanostructure is operated at much heavier loads. Thus, the dissolution and collapse might be initiated from the top and then propagate to the bottom region.

This geometric effect is also observed in the local OH^- ion concentration as shown by Fig. 4e–h. The region with a higher curvature induces ion migration and concentrates OH^- ions due to the electric field and possibly facilitated by the faster reaction rate and the resulting mass diffusion/convection. This ion aggregation does not necessarily mean the local pH value at the tip is higher since the consumption of OH^- during the OER might proceed at an even higher rate. This speculation is supported by the fact that the local OH^- ion concentration is less than 10 times higher at the tip where the reaction rate can be 20 times higher (*cf.* local current density in Fig. 4a). In this scenario, the lower local pH destabilizes the oxyhydroxide at high anodic potentials, promoting the dissolution of metal ions. Remarkably, such ion aggregation is not significant in CoNi-900-800 where the distribution of OH^- is roughly uniform across the surface.

Such FEA partially explains the tendency that the tip region is prone to dissolution due to the harsher reaction environment. Yet, it remains unclear why these model catalysts, all with

tip/top regions, show contrasting structural stability. In fact, cobalt oxyhydroxide catalysts often feature reactive lattice oxygens (LOs) during the OER, which thus follows the lattice oxygen mechanism (LOM).^{30,31} Compared with the conventional adsorbate evolution mechanism (AEM), this pathway enjoys favored OER kinetics due to the circumvention of thermodynamic constraints brought by the scaling relationship, yet is notorious for the detrimental effect of metal center dissolution due to the fast LO exchange.³² We thus explored whether the LO reactivity is affected by the nanostructure, which eventually causes the stability difference.

In the LOM, the peroxo ($^*\text{O}_2^{2-}$) ligand on the surface is the key intermediate which differs from the commonly observed superoxo ($^*\text{O}^{2-}$) ligand in the AEM. It is formed through the combination of lattice oxygen and the adsorbed oxygen atom, which is thermodynamically more stable than the superoxo ligand (see Fig. 5a). Previous studies show that the tetramethylammonium ion (TMA^+) in the electrolyte can strongly bind the peroxo group during the OER process, inhibiting the subsequent diatomic oxygen release and LO refilling. Thus, the OER kinetics is greatly impaired. Such effect is not prominent with the superoxo ($^*\text{O}^{2-}$) ligand in the AEM. We thus used TMA^+ cations as the probe to evaluate the LO reactivity among the model catalysts. Fig. 5b shows the LSVs obtained in 1 M KOH with and without 1 M tetramethylammonium hydroxide (TMAOH). Interestingly, the voltammograms of CoNi-900-800 in both electrolytes are essentially identical, whereas those of CoNi-750-50 shows apparent difference. This indicates that the LOM pathway prevails in the CoNi-750-50 catalyst.

To further validate the distinct LO reactivities among various nanostructures, we explored the proton–electron transfer kinetics by evaluating the OER activity in electrolytes with different pH values. Such pH-dependent OER activity is often used to determine the reaction order with respect to proton activity. To avoid the use of buffers and additives, which maintain a stable local pH on the catalyst surface during the OER or keep the ionic strength constant, we selected the pH

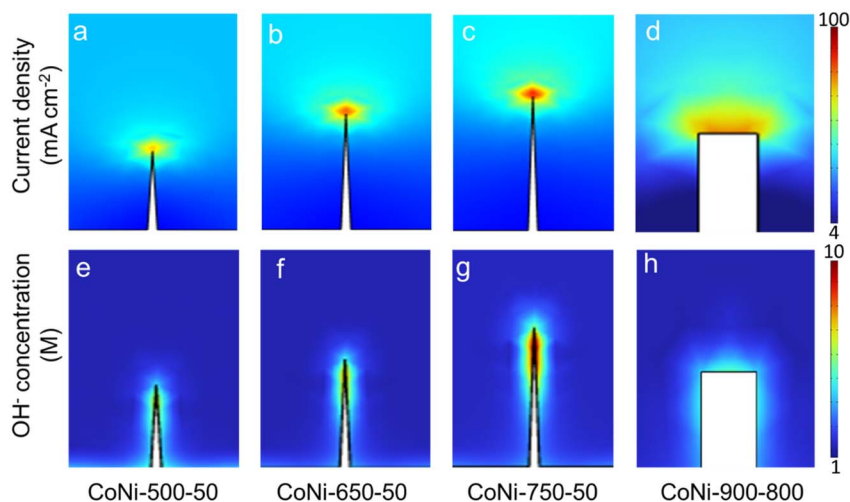


Fig. 4 (a–d) Local current density distribution and (e–h) local OH^- ion concentration distribution among various model catalysts.

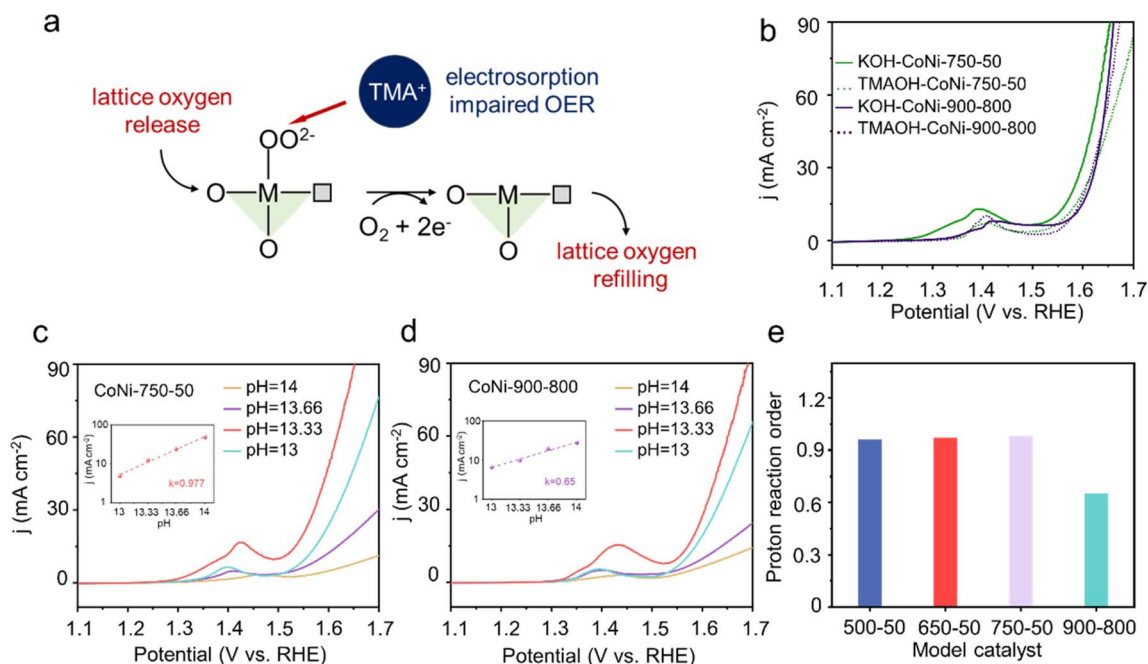


Fig. 5 (a) The schematic mechanism of the TMA^+ probe study of lattice oxygen reactivity in the OER; (b) LSV plots of model catalysts obtained in 1 M KOH with and without 1 M TMA^+ ; (c–e) pH dependence and proton reaction order of model catalysts.

range in the strong alkaline domain (pH = 14, 13.6, 13.3, and 13). This is because the additional electrolyte components might not be sufficiently inert and interfere with the accurate determination of the intrinsic OER activity of our model catalysts.³³ The proton reaction order is then obtained by measuring the current density at a fixed potential as a function of pH using $\partial \log(j)/\partial \text{pH}$, as shown in eqn (3) below on an RHE scale.

$$\rho_{\text{RHE}} = \partial \log(j)/\partial \text{pH} \quad (3)$$

As shown in Fig. 5c, the OER performance of CoNi-750-50 varies substantially in different electrolytes, the calculated proton reaction order reaches 0.98, implying the that the LOM might dominate in the reaction. While CoNi-900-800 also shows pH-dependent OER performance in Fig. 5d, the proton reaction order is 0.65, indicative of the prevailing role of AEM. A summary of the reaction order is shown in Fig. 5e, which demonstrates that all the nanorod model catalysts feature highly reactive LOs, contrasting that of the nanosheet structure, during the OER. This causes dramatic structural disintegration of the nanorod during the longevity test.

To quantitatively study the LO reactivity of all model catalysts during the OER, we finally carried out a differential electrochemical mass spectrometric (DEMS) study coupled with ^{18}O isotopic labeling (see Fig. 6a). All catalysts are initially subjected to a high anodic potential in 1 M KOH using H_2^{18}O as the solvent. This enables the oxygen exchange, if any, with the lattice where the ^{18}O isotope is incorporated on the surface.³⁴ These labeled catalysts are then tested in the DEMS setup in 1 M KOH using H_2^{16}O as the solvent where the evolution of different isotopic diatomic oxygens is monitored under *operando* conditions.³⁵ Fig. 6b and c compare the ionic signals at $m/z = 32$ and

34 corresponding to $^{32}\text{O}_2$ and $^{34}\text{O}_2$, respectively, of CoNi-750-50 and CoNi-900-800. CoNi-750-50 shows strong signals of both $^{32}\text{O}_2$ and $^{34}\text{O}_2$. The $^{34}\text{O}_2/^{32}\text{O}_2$ ratio reaches 17.26%, confirming the substantial involvement of lattice oxygen during the OER. Inversely, a strong signal of $^{32}\text{O}_2$ is recorded, while that of $^{34}\text{O}_2$ is negligible in CoNi-900-800. The $^{34}\text{O}_2/^{32}\text{O}_2$ ratio is only 0.16%, close to the natural abundance of ^{18}O , reflecting the inert nature of lattice during the OER.

Since a higher $^{34}\text{O}_2/^{32}\text{O}_2$ ratio indicates more surface lattice oxygens participate in the OER, or a higher LO exchange rate during the reaction, we thus used the $^{34}\text{O}_2/^{32}\text{O}_2$ ratio as the descriptor of LO reactivity in the OER. Fig. 6d compares this value among different catalysts. Indeed, all nanorod structures demonstrate notable LO reactivity and LOM in the OER, as evidenced by the high $^{34}\text{O}_2/^{32}\text{O}_2$ ratio. The value of this ratio follows the order of NiCo-500-50 > NiCo-650-50 > NiCo-750-50, suggesting that the LO reactivity follows the same order. We then can conclude that all carbonate hydroxide pre-catalysts, irrespective of the nanostructures, are reconstructed to oxyhydroxides during the OER. Because of the distinct nanostructures which might feature different surface chemistries such as defects, facet orientation and metal–oxygen covalency,³⁶ these resulting oxyhydroxides show nanostructure-dependent LO reactivity. The high LO reactivity in NiCo-500-50 promotes metal dissolution and causes rapid structural disintegration. NiCo-750-50, however, is more robust and suffers dissolution at the tip due to lower LO reactivity. Although NiCo-900-800 shares the identical chemical composition with the nanorod counterparts, yet shows little LO reactivity. It is thus the most stable catalyst during the OER. Therefore, such nanostructure-dependent LO reactivity correlates well with the trend of structural degradation.

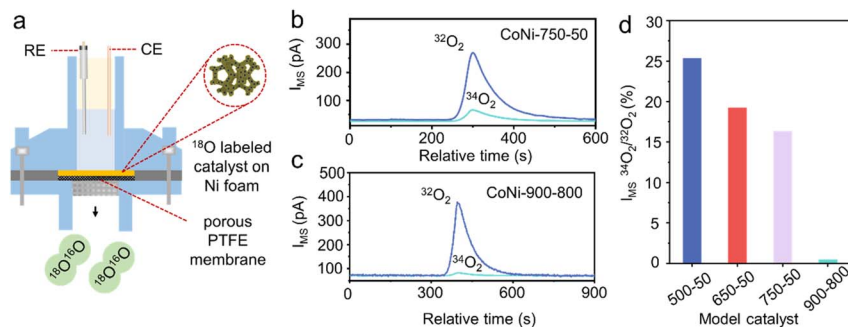


Fig. 6 (a) The schematic illustration of the DEMS cell to probe the isotopically labeled OER model catalyst on Ni foam; (b and c) the DEMS signal comparison during the OER; (d) comparison of the $^{34}\text{O}_2/^{32}\text{O}_2$ ratio among model catalysts.

4. Conclusion

Using a series of nanostructured model electrocatalysts with different aspect ratios and various *operando* characterization approaches, we show the structure-dependent lattice oxygen reactivity and the strongly correlated degree of structural degradation during the OER process. Finite element analysis indicates that a high curvature structure leads to high local current density, resulting in a harsher reaction environment that exacerbates the electrode corrosion. In the future, more work should be examined to understand if such structure-dependent lattice oxygen reactivity is also applicable in other OER catalysts. Our results reveal a possible degradation pathway for nanostructured electrocatalysts, offering guidelines for developing robust nanomaterials for real-life applications.

Data availability

The data that support the findings of this study are available from the corresponding author, N. Yan, upon reasonable request.

Conflicts of interest

The authors declare that they have no known competing financial interests.

Acknowledgements

We acknowledge the funding from the National Natural Science Foundation of China (52272233), Guangdong Basic and Applied Basic Research Foundation (2023A1515011161) and the Netherlands Organization for Scientific Research (NWO) Vidi grant (VI.Vidi.192.045).

References

- S. Chu and A. Majumdar, Opportunities and challenges for a sustainable energy future, *Nature*, 2012, **488**, 294–303.
- B. You, M. T. Tang, C. Tsai, F. Abild-Pedersen, X. Zheng and H. Li, Enhancing electrocatalytic water splitting by strain engineering, *Adv. Mater.*, 2019, **31**, 1807001.
- R. Fan, C. Liu, Z. Li, H. Huang, J. Feng, Z. Li and Z. Zou, Ultrastable electrocatalytic seawater splitting at ampere-level current density, *Nat. Sustainability*, 2024, **7**, 158–167.
- S. Perumal, I. Pokhrel, U. Muhammad, X. Shao, Y. Han, M. Kim and H. Lee, Recent advances in electrochemical water splitting electrocatalysts: categorization by parameters and catalyst types, *ACS Mater. Lett.*, 2024, **6**, 3625–3666.
- M. Yu, E. Budiyo and H. Tüysüz, Principles of water electrolysis and recent progress in cobalt-, nickel-, and iron-based oxides for the oxygen evolution reaction, *Angew. Chem., Int. Ed.*, 2021, **61**, e202103824.
- L. Bai, S. Lee and X. Hu, Spectroscopic and electrokinetic evidence for a bifunctional mechanism of the oxygen evolution reaction, *Angew. Chem., Int. Ed.*, 2020, **60**, 3095–3103.
- Y. Jia, K. Jiang, H. Wang and X. Yao, The role of defect sites in nanomaterials for electrocatalytic energy conversion, *Chem*, 2019, **5**, 1371–1397.
- Y. Zhu, W. Liang, C. Zhang, F. Bin and Q. Tao, Defect-rich regulatory activity strategy: disordered structure for enhanced catalytic interfacial reaction of chlorobenzene, *Environ. Sci. Technol.*, 2024, **58**, 19385–19396.
- P. Muhammad, A. Zada, J. Rashid, S. Hanif, Y. Gao, C. Li, Y. Li, K. Fan and Y. Wang, Defect engineering in nanocatalysts: from design and synthesis to applications, *Adv. Funct. Mater.*, 2024, **34**, 2314686.
- Y. W. Choi, H. Mistry and B. Roldan Cuenya, New insights into working nanostructured electrocatalysts through *operando* spectroscopy and microscopy, *Curr. Opin. Electrochem.*, 2017, **1**, 95–103.
- Y. S. Byeon, W. Lee, S. Park, D. Kim, J. Jung, M. S. Park and W. S. Yoon, Comprehensive understanding of elemental doping and substitution of Ni-Rich cathode materials for lithium-ion batteries via *In situ operando* analyses, *Small Sci.*, 2024, **4**, 2400165.
- F. Zeng, C. Mebrahtu, L. Liao, A. K. Beine and R. Palkovits, Stability and deactivation of OER electrocatalysts: A review, *J. Energy Chem.*, 2022, **69**, 301–329.
- F.-Y. Chen, Z.-Y. Wu, Z. Adler and H. Wang, Stability challenges of electrocatalytic oxygen evolution reaction:

- From mechanistic understanding to reactor design, *Joule*, 2021, 5, 1704–1731.
- 14 Z. Pei, H. Zhang, D. Luan and X. W. Lou, Electrocatalytic acidic oxygen evolution: From catalyst design to industrial applications, *Matter*, 2023, 6, 4128–4144.
 - 15 T. Kou and Y. Li, Catalyst deactivation in alkaline water splitting, *Sci. China: Chem.*, 2022, 66, 301–303.
 - 16 Z. Kou, X. Li, L. Zhang, W. Zang, X. Gao and J. Wang, Dynamic surface chemistry of catalysts in oxygen evolution reaction, *Small Sci.*, 2021, 1, 2007377.
 - 17 Y. Sun, C.-R. Wu, T.-Y. Ding, J. Gu, J.-W. Yan, J. Cheng and K. H. L. Zhang, Direct observation of the dynamic reconstructed active phase of perovskite LaNiO₃ for the oxygen-evolution reaction, *Chem. Sci.*, 2023, 14, 5906–5911.
 - 18 X. Y. Zhang, H. Yin, C. C. Dang, H. Nie, Z. X. Huang, S. H. Zheng, M. Du, Z. Y. Gu, J. M. Cao and X. L. Wu, Unlocking enhanced catalysis stability in acidic oxygen evolution: structural insights for PEM applications under high-current density, *Angew. Chem., Int. Ed.*, 2025, 64, e20242556.
 - 19 H. Zhong, Q. Zhang, J. Yu, X. Zhang, C. Wu, Y. Ma, H. An, H. Wang, J. Zhang, X. Wang and J. Xue, Fundamental Understanding of Structural Reconstruction Behaviors in Oxygen Evolution Reaction Electrocatalysts, *Adv. Energy Mater.*, 2023, 13, 202301391.
 - 20 X. Cao, R. Chen, Z. Wang, H. Feng, Q. Zhang and N. Yan, In situ reactivating perovskite oxide catalysts in alkaline water electrolyzers: a generalized approach based on selective cation leaching, *ACS Sustainable Chem. Eng.*, 2023, 11, 16693–16702.
 - 21 T. Binninger, R. Mohamed, K. Waltar, E. Fabbri, P. Levecque, R. Kötz and T. J. Schmidt, Thermodynamic explanation of the universal correlation between oxygen evolution activity and corrosion of oxide catalysts, *Sci. Rep.*, 2015, 5, 12167.
 - 22 H. Du, H. Luo, M. Jiang, X. Yan, F. Jiang and H. Chen, A review of activating lattice oxygen of metal oxides for catalytic reactions: Reaction mechanisms, modulation strategies of activity and their practical applications, *Appl. Catal., A*, 2023, 664, 119348.
 - 23 A. Grimaud, O. Diaz-Morales, B. Han, W. T. Hong, Y.-L. Lee, L. Giordano, K. A. Stoerzinger, M. T. M. Koper and Y. Shao-Horn, Activating lattice oxygen redox reactions in metal oxides to catalyse oxygen evolution, *Nat. Chem.*, 2017, 9, 457–465.
 - 24 X. Yan, Y. Zhao, J. Biemolt, K. Zhao, P. C. M. Laan, X. Cao and N. Yan, “Nano-garden cultivation” for electrocatalysis: controlled synthesis of Nature-inspired hierarchical nanostructures, *J. Mater. Chem. A*, 2020, 8, 7626–7632.
 - 25 X. Jiang, K. Zhao, H. Feng, L. Ke, X. Wang, Y. Liu, L. Li, P. Sun, Z. Chen, Y. Sun, Z. Wang, L. Yu and N. Yan, Unraveling side reactions in paired CO₂ electrolysis at operando conditions: a case study of ethylene glycol oxidation, *J. Am. Chem. Soc.*, 2025, 147, 13471–13482.
 - 26 S. Hussain, T. Liu, M. Kashif, L. Lin, S. Wu, W. Guo, W. Zeng and U. Hashim, Effects of reaction time on the morphological, structural, and gas sensing properties of ZnO nanostructures, *Mater. Sci. Semicond. Process.*, 2014, 18, 52–58.
 - 27 M. Uwaha, *Handbook of Crystal Growth*, Elsevier, 2015, pp. 359–399.
 - 28 P. Liu, B. Chen, C. Liang, W. Yao, Y. Cui, S. Hu, P. Zou, H. Zhang, H. J. Fan and C. Yang, Tip-enhanced electric field: a new mechanism promoting mass transfer in oxygen evolution reactions, *Adv. Mater.*, 2021, 33, 2007377.
 - 29 K. Tong, W. Qiu, S. Zhang, W. Zhao, P. Wu, F. Lin, L. Chu, H. Wang, W. Tian and M. Huang, Wide-area tip-like effect boosting electrocatalytic sulfion oxidation for energy-efficient hydrogen production in seawater electrolysis, *Chem. Eng. J.*, 2025, 510, 161611.
 - 30 Z.-F. Huang, J. Song, Y. Du, S. Xi, S. Dou, J. M. V. Nsanzimana, C. Wang, Z. J. Xu and X. Wang, Chemical and structural origin of lattice oxygen oxidation in Co-Zn oxyhydroxide oxygen evolution electrocatalysts, *Nat. Energy*, 2019, 4, 329–338.
 - 31 J. Zhao, Y. Zhang, Y. Ye, Q. Xu, S. Luo, F. Meng, S. Zhu, X. Li, X. Lin, A. Yu, X. Ren, T. Wu and Z. J. Xu, Remote Iron dynamics of NiFe (oxy)hydroxides toward robust active sites in water oxidation, *Nat. Commun.*, 2025, 16, 5601.
 - 32 J. Song, C. Wei, Z.-F. Huang, C. Liu, L. Zeng, X. Wang and Z. J. Xu, A review on fundamentals for designing oxygen evolution electrocatalysts, *Chem. Soc. Rev.*, 2020, 49, 2196–2214.
 - 33 L. Giordano, B. Han, M. Risch, W. T. Hong, R. R. Rao, K. A. Stoerzinger and Y. Shao-Horn, pH dependence of OER activity of oxides: Current and future perspectives, *Catal. Today*, 2016, 262, 2–10.
 - 34 K. Zhao, X. Jiang, X. Wu, H. Feng, X. Wang, Y. Wan, Z. Wang and N. Yan, Recent development and applications of differential electrochemical mass spectrometry in emerging energy conversion and storage solutions, *Chem. Soc. Rev.*, 2024, 53, 6917–6959.
 - 35 K. Zhao, S. Han, L. Ke, X. Wu, X. Yan, X. Cao, L. Li, X. Jiang, Z. P. Wang, H. J. Liu and N. Yan, Operando studies of electrochemical denitrogenation and its mitigation of N-doped carbon catalyst in alkaline media, *ACS Catal.*, 2023, 13, 2813–2821.
 - 36 P.-C. Yu, X.-L. Zhang, T.-Y. Zhang, X.-Y.-N. Tao, Y. Yang, Y.-H. Wang, S.-C. Zhang, F.-Y. Gao, Z.-Z. Niu, M.-H. Fan and M.-R. Gao, Nitrogen-mediated promotion of cobalt-based oxygen evolution catalyst for practical anion-exchange membrane electrolysis, *J. Am. Chem. Soc.*, 2024, 146, 20379–20390.